

Relevance of ExB Drifts for Particle and Heat Transport in Divertors

C.K. Tsui¹, J.A. Boedo¹, O. Février², H. Reimerdes², C. Colandrea², S. Gorno², and the TCV Team^a

¹ Center for Energy Research, University of California San Diego (UCSD), La Jolla, USA

²Ecole Polytechnique Fédérale de Lausanne (EPFL), Swiss Plasma Center (SPC), CH-1015 Lausanne Switzerland

^aSee the author list of S. Coda et al 2019 Nucl. Fusion 59 112023

E-mail: C7tsui@UCSD.edu

Abstract

Radial electric fields up to $\sim 4\text{kV/m}$ are observed in the boundary between the private flux region (PFR) and the Scrape-off Layer (SOL) driving ExB drifts between the inner and outer targets at speeds up to 2.8km/s in the TCV divertor. The resulting ExB fluxes, located in a narrow region ($\Delta\rho_\psi < 0.012$ in normalized radius or $\Delta R-R_{\text{sep}} < 4\text{mm}$ mapped to the outer midplane) are equivalent to around 20% of the total heat and particle flux to the divertor targets (inner + outer). At the peak E_r , the ExB poloidal transport is equivalent to parallel flows with $M_\parallel \sim 3$. In the snowflake divertor with a second X-point in the outer SOL, the drifts in the PFR-SOL boundary were equivalent to around 30% of the total heat and particle flux to the divertor targets and cover a region $\sim 50\%$ wider than in the single null ($\Delta\rho_\psi \sim 0.016$, $\Delta R-R_{\text{sep}} \sim 6\text{mm}$). The location of the PFR-SOL boundary drift shifts radially in the $E_\parallel \times B$ direction when reversing the toroidal field direction. Peaks in density and electron pressure have been identified near the primary X-point along with large gradients in density, temperature, and potential, the latter resulting in a local electric field $\sim 2.7\text{kV/m}$ which drives a drift (1.9km/s) upwards towards the closed flux surfaces. Floating potential (V_f) magnitudes up to 75V ($\sim 2kT_e$) were measured, indicating that V_f and parallel currents should not be neglected when estimating plasma potential.

Keywords: Tokamak, Divertor, Scrape-Off Layer, TCV, Target Asymmetry

(Some figures may appear in color only in the online journal)

1 Introduction

Understanding, predicting, and managing the large heat and particle fluxes in future tokamak divertors is critical for the success of future fusion reactors [1–3]. One of the important mechanisms affecting the behavior of the divertor is the ExB drift circulation (see black arrows Figure 1). These drifts were identified as being the most likely cause of the changes to the inner and outer divertor plasma conditions when reversing the direction of the toroidal field B_t [4–6], and later quantified numerically [7–10] and experimentally [11–14] to play an important role in driving convective flows through the divertor [15–23]. The ExB convection occurring in the boundary between the scrape-off layer (SOL) and the private flux region (PFR) [red arrow in Figure 1] is thought to be especially important as the drifts in this region connect the two divertor targets and have been shown to convect 25–40% of the total ion flow to the divertor [12–14]. More recently, drifts have also been identified as a key player at the onset of detachment, where the reduction in temperature reduces the electric fields and this PFR-SOL boundary drift, resulting in a bifurcated transition to

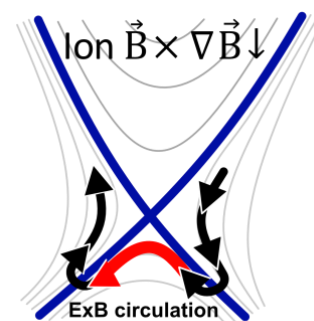


Figure 1 Diagram of the ExB circulation pattern in forward field thought to be ubiquitous in divertor tokamaks. This paper will focus on the region shown by the red arrow.

strongly detached outer divertor conditions when the ion $B \times \nabla B$ drift points towards the X-point [24–27]. ExB drifts are also important when considering impurity transport [28–30].

ExB drifts have also been shown to be important in alternative divertor configurations such as the Snowflake[31,32]. The Low-Field Side Snowflake Minus divertor configuration exploits changes in magnetic geometry with the aim to reduce and/or provide better control over target fluxes [33–43] by using two nearby divertor X-points. Recent work shows that this divertor configuration outperforms the single null, distributing the outer-target heat flux over $\sim 2\times$ the wetted area [44]. This broadening was not reproduced in fluid simulations without drifts [41,42], possibly because much of the heat flux in the broadened SOL is carried by $E_r \times B$ drifts [45].

This study expands on previous direct measurements of the electric fields and resulting drifts in the divertor [11–14,45] by using a reciprocating probe in a Single Null divertor (SN) and a Low-Field Side Snowflake minus divertor (hereafter referred to simply as the snowflake) in the TCV tokamak to provide high spatial resolution measurements of plasma potential, electron temperature T_e , and density n_e in order to investigate the role of plasma convection due to ExB drifts and parallel flows. The current study quantifies heat and particle fluxes and confirm that the PFR-SOL boundary harbors a key mechanism driving in-out asymmetry in the divertor and shows that the ExB drifts dominate over convective parallel transport, thus deserving dedicated attention when describing and designing divertor solutions. Studies with the snowflake geometry will show that drift driven convection can be modified by the secondary separatrix, suggesting that the ExB circulation pattern can be potentially modified and exploited.

2 Experimental Setup

The discharges utilized in these experiments are ohmically heated, in L-mode, and take advantage of the flexibility of the Tokamak à Configuration Variable (TCV)[46] to diagnose the single null and the snowflake shown in Figure 2. The plasma discharges featured forward Bt and Ip (toroidal field Bt = -1.44T, ion $B \times \nabla B$ downward, plasma current Ip = - 235 +/- 10 kA) or reversed Bt and Ip (Bt = 1.44T, $B \times \nabla B$ upward, Ip = 235 +/- 10 kA). The line-integrated electron density was held constant via feedback control at $\langle n_e \rangle \sim 3.8e19 \pm 0.4e19 \text{ m}^{-3}$, i.e. at a Greenwald fraction of ~ 0.25 in attached conditions with collisionality values ($\nu_{sol}^* = 10^{-16} n_e L_{\parallel} / T_e^2 \sim 25$) typical of the conduction limited regime where parallel heat fluxes are thought to be dominated by electron heat conduction and where target temperatures are low. An example time evolution of the core plasma parameters is shown in Figure 3 showing that the plasma is well controlled during the stationary phases for the snowflake (pink region) and the single null (blue region).

Figure 2 shows the equilibrium reconstruction for the single null divertor and the snowflake in the left and right panels respectively. The measurement locations are shown for the Thomson scattering[47], the wall Langmuir probes[48,49], the Horizontal Infrared Camera, and the fast reciprocating probe[50]. The plasmas were moved up and down while minimizing shape changes, granting reciprocating probe access to multiple vertical slices up to the primary X-point. Where possible, the strike points were located on vertical targets so that moving the plasma up or down did not change the neutral recycling. The slices are 20cm in the R direction at Z=-46cm as shown by the black horizontal line. One of the main differences between the present study and ref [45] is the location of the reciprocating probe, and the deeper plunge depth, which was facilitated using a longer graphite shroud and probe shaft assembly.

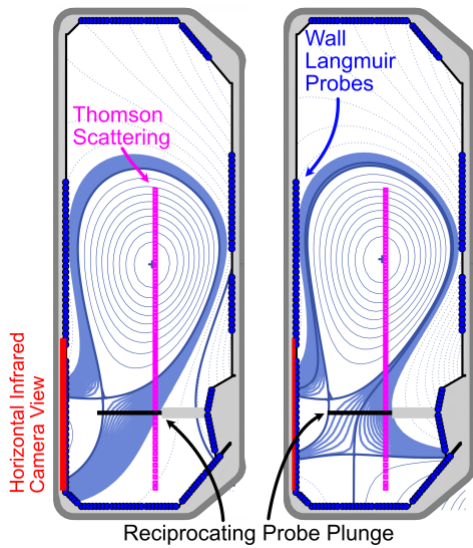


Figure 2 The poloidal cross-section of the TCV vessel with two example equilibrium reconstructions of a single null (left) and a snowflake divertor (right) from discharge 66844. The measurement location of the horizontal reciprocating probe is shown in black. The Thomson scattering, IR camera, and wall Langmuir probes measurement positions are shown by the magenta squares, red bar, and blue circles respectively.

Example Time Evolution 66844

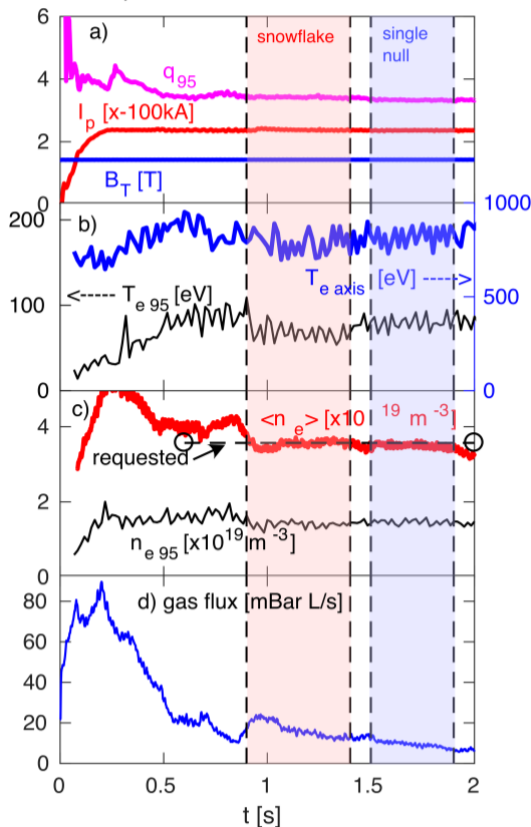


Figure 3 Example time evolution of TCV discharge 66844. Ramp up and shape development occurred until $t=0.9$ s, then machine conditions were maintained constant during the snowflake phase (pink region) and the single null phase (blue region). Time traces are plotted for (a) q_{95} , I_p , B_T (b) T_e at the magnetic axis (right axis) and at the $\rho=0.95$ surface (left axis) (c) the line average density $\langle n_e \rangle$ (red) compared to the requested value, n_e at the $\rho=0.95$ surface, and (d) the neutral gas flux.

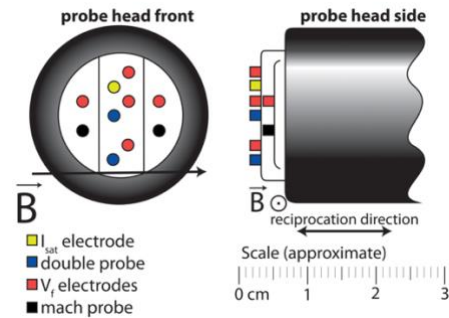


Figure 4 A diagram of the head of the reciprocating probe illustrating the geometry and orientation of the electrodes, which are color coded depending on their function.

The reciprocating probe head is equipped with 10 electrodes (as shown in Figure 4) which were operated in distinct diagnostic clusters, in order to measure various plasma parameters. The probe head was rotated to an angle of 0° (i.e. flat. See in Figure 4 left). For the plasma geometries in this study, the field-lines intersecting the probe were toroidally aligned within 4° such that shadowing from the adjacent electrodes or from the probe structure was negligible and the projected surface areas could be taken as constant. T_e , n_e and electron pressure ($p_e = n_e k T_e$) were measured using the double probe technique with a $\pm 300V$ triangular wave with a sweep frequency of 1kHz and digitized at 10 MS/s. The values in this paper are error-weighted means collected over 5ms unless stated otherwise.

The Mach number M_\parallel was determined following the procedure in ref [51] using the electrodes shaded in black in Figure 4. The electrodes labeled V_f (red) were used to measure the floating potential, and the plasma potential V_p was calculated as $V_p = V_f + 2.5kT_e$. While parallel flows and cross-field $E_r \times B$ drifts act in orthogonal directions, they both transport plasma towards or away from the target. In order to compare their relative contributions, the particle and heat fluxes are projected in the poloidal direction and mapped to the OMP by correcting for poloidal and total flux expansion.

The poloidal projection of the parallel particle flux with corrections for flux expansion is defined as:

$$\Gamma_\theta^\parallel = \frac{B_{\theta \text{ OMP}}}{B_\theta} \sin(\alpha) n_e c_s M_\parallel \quad (1)$$

where c_s is the sound speed, $B_{\theta \text{ OMP}}$ and B_θ are the poloidal magnetic flux densities at the OMP and at the measurement location respectively. α is the field line angle such that $\sin \alpha \equiv B_\theta / B_\parallel$.

Radial electric fields calculated using OMP flux coordinate $R - R_{\text{sep}}$:

$$f_x E_r = \frac{-dV_p}{d(R - R_{\text{sep}})} \quad (2)$$

which is used for the poloidal projection of the $E_r \times B$ flux:

$$\Gamma_\theta^{E_r \times B} = \frac{B_{\phi \text{ OMP}}}{B_\phi} \cos(\alpha) \cdot \frac{n_e}{B_\parallel} \frac{-dV_p}{d(R - R_{\text{sep}})} \quad (3)$$

A divergence-free $E_r \times B$ will have constant $\Gamma_\theta^{E_r \times B}$ in the poloidal direction [52,53].

The amount of heat convected by these mechanisms q_θ^\parallel and $q_\theta^{E_r \times B}$ are calculated assuming that $T_i = T_e$ as

$$q_\theta = \Gamma_\theta \left(5kT_e + \frac{1}{2} m_i v_\parallel^2 + \epsilon_{\text{pot}} \right) \quad (4)$$

where the recombination energy for D_2 $\epsilon_{\text{pot}} = 15.8\text{eV}$, though this term is negligible for the range of temperatures in this manuscript.

These fluxes can be integrated over any region using:

$$\dot{N} = \int_a^b 2\pi R_{\text{OMP}} \Gamma_\theta d(R - R_{\text{sep}}) \quad (5)$$

$$P = \int_a^b 2\pi R_{\text{OMP}} q_\theta d(R - R_{\text{sep}}) \quad (6)$$

3 Gradients at the Separatrix and throughout the SOL

3.1 Single Null Divertor

Reciprocating probe data are presented for identical LSN shapes in reversed and forward fields in Figure 5 and Figure 6 respectively in order to highlight the effects of ExB drifts in the divertor. The reverse field LSN equilibrium reconstruction is shown in Figure 5-left with the probe trajectories overlaid. Example error bars have been included to select datapoints to indicate the typical $\pm 2\sigma$ scatter in the SOL data before averages were taken over 2ms intervals.

The plasma potential V_p features a large gradient across the separatrix at the PFR-SOL boundary, as seen in Fig. 5e, produced by a $\sim 55V$ increase over $\sim 1mm$, ($f_x E_r \sim 40$ kV/m) which drives a strong ExB drift downwards and towards the outer target in this field direction. Since V_p is calculated from V_f (5-d) and T_e (5-b), note that both quantities show gradients in the same region that combine to create the observed E_r field. V_f magnitudes on the order of kT_e were measured indicating that V_f and parallel currents cannot be neglected when evaluating V_p . V_p drops gradually across the SOL representing a weaker E_r which drives an ExB drift upwards away from the outer target. The directions of the $E_r \times B$ drifts are indicated by the red arrows in Figure 5-left.

The Mach number (fig. 5f) changes directions at the separatrix, with the $M_{\parallel} < 0$ sign indicating (in this helicity) flow away from the outer target. The parallel flow opposes the ExB drifts, convecting particles away from the outer target in the PFR, and towards the outer target in the SOL. In section 4, it will be shown that the ExB drift in the PFR-SOL boundary dominates over the opposing $M_{\parallel} = -0.75$ flow.

The peak in n_e (fig. 5a) in the divertor occurs at R-Rsep $\sim 1-3mm$; i.e. shifted radially outward with respect to the separatrix and the peak in T_e , consistent with the direction of the $E_{\parallel} \times B$ drift.

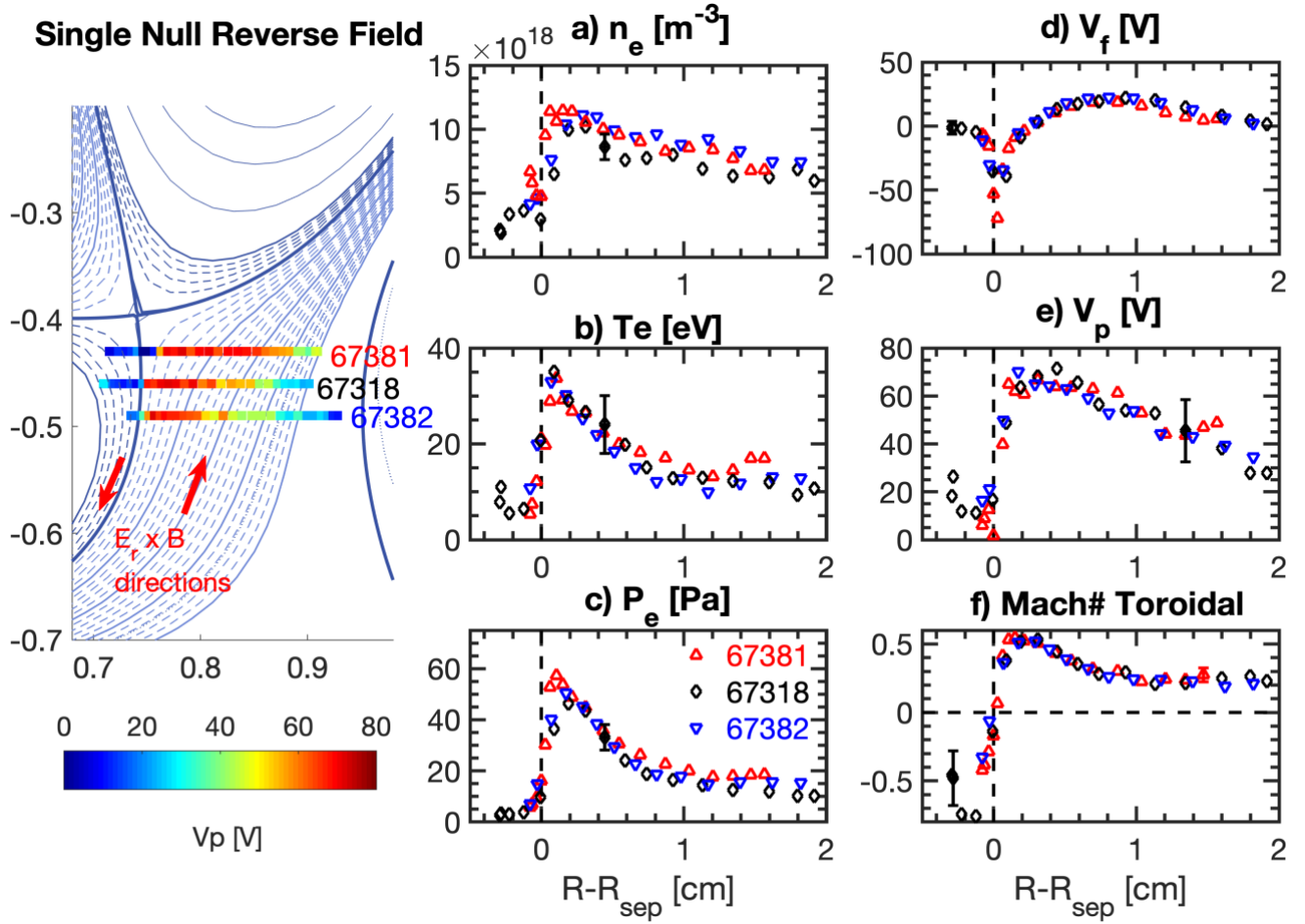


Figure 5 2D reciprocating probe profiles in the reverse field single null. The equilibrium (left) indicates the plunge locations for each shot number. The SOL is demarcated with 1mm flux surfaces by the dashed and solid lines from up to $R-R_{sep} = 2.0$ cm. The colorbar indicates V_p along the probe plunges, and the red arrows indicate the approximate directions of the $E_r \times B$ drifts. The profiles (right) color coded according to the sampled trajectory, show the interval averaged electron density n_e (a), electron temperature T_e (b), electron pressure P_e (c), floating potential V_f (d), plasma potential V_p (e) and Mach number $M_{||}$ (f) as a function of the flux coordinate $R-R_{sep}$. The error-bars represent the typical $\pm 2\sigma$ scatter in the data before the averages were taken.

Four slices were taken across the forward field single null divertor, two of which intersected with the X-point as shown in the equilibrium reconstruction in Figure 6 left. A key result again is the steep gradient in the V_p profile at the PFR-SOL boundary (fig 6e), resulting in a significant $f_x E_r \sim 30$ kV/m. The decreased peak and flatter gradients compared to the reverse field case are a result of V_f (fig 6d) which is negative throughout the SOL, mirroring the T_e profile (fig 6b). This results in a narrower region of high E_r rather than a reduction in the V_p profile gradient (more details in section 4). In this field orientation, the $E_r \times B$ drift in the PFR-SOL boundary convects particles away from the outer target and towards the inner target, while in the SOL, the drifts convect towards the outer target (see red arrows in Figure 6 left). The $M_{||}$ profiles (fig 6f) indicate flow towards the outer target in the SOL and the PFR (66844 and 66803 profiles enter the PFR).

The n_e profiles below the X-point (66844 and 66803) have peaks which are shifted with respect to the separatrix in the direction of the $E_r \times B$ drift, this time shifting radially inward into the PFR to $R-R_{sep} \sim -2$ mm. This results in a 6-fold change in the density in the PFR just below the X-point with no change in T_e when fields are reversed (Compare Fig 5a and 6a at $R-R_{sep} = -2$ mm).

Across the SOL the n_e profiles show a poloidal density gradient, where n_e increases while approaching the target, i.e., the uppermost n_e profile (red up triangles) has values $\sim 40\%$ lower than the lowermost (green down triangles). A corresponding drop in T_e is not observed while approaching the target (Fig 5b) resulting in a small increase in p_e (Fig 6c), albeit a small one compared to the scatter in the measurements.

Two of the reciprocating probe plunges (66841 and 67312) approach the primary X-point and traverse a 5cm wide region where, due to flux expansion, the normalized coordinate remains essentially constant ($|R-R_{sep}| \leq 1\text{mm}$). Within this region, a large increase of $\times 4$ in n_e (Fig 6a) occurs along with a similar decrease in T_e (Fig 6b). This feature will be discussed at length in the dedicated section 5. Note that a drop in V_p (Fig 6e) and a sign reversal in $M_{||}$ (Fig 6f) also occur near the X-point likely indicating that the probe has crossed over to closed flux surfaces (where $M_{||} < 0$ would point co-Ip), or to the inner divertor where $M_{||} < 0$ would point to the inner target.

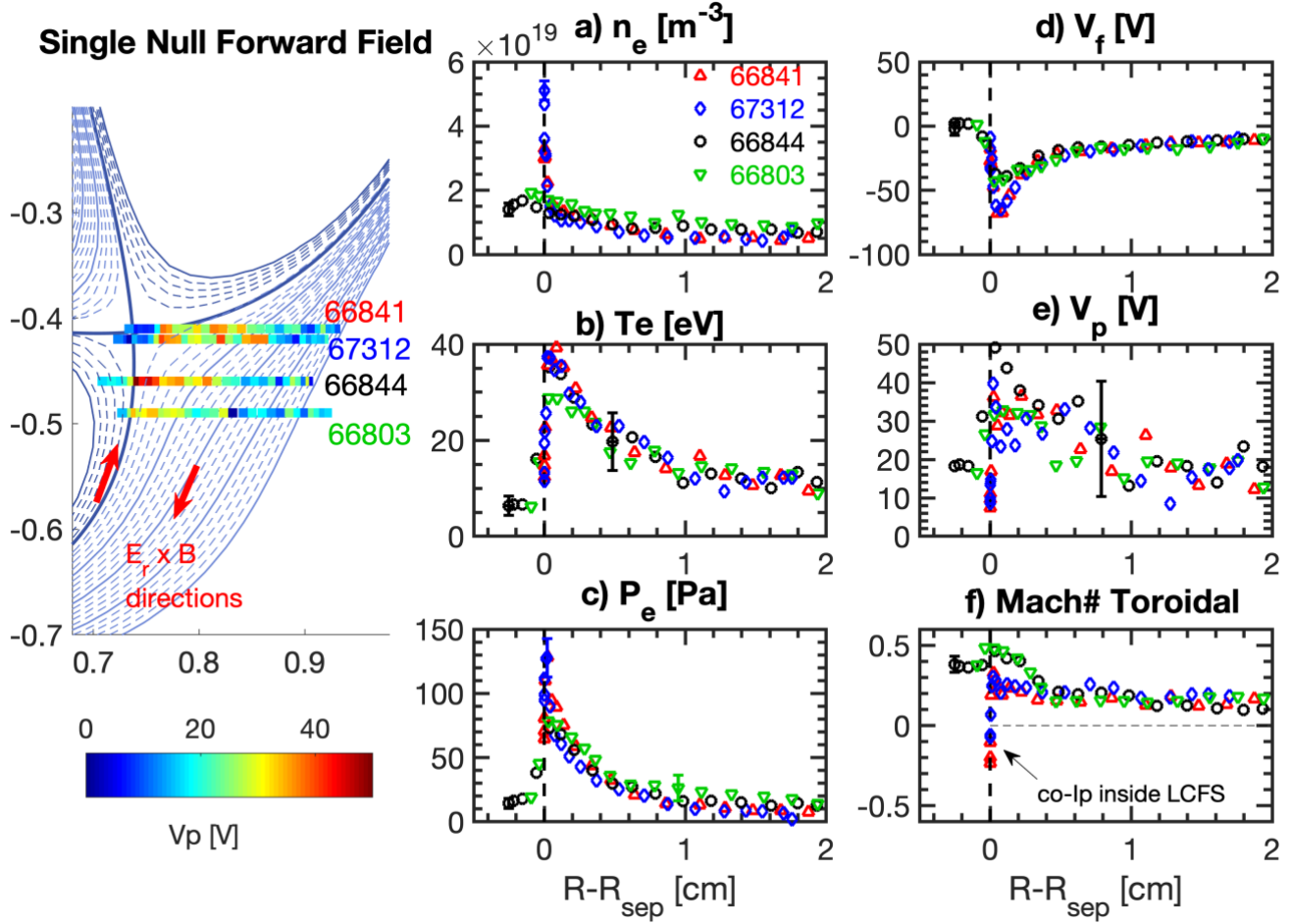


Figure 6 2D reciprocating probe profiles in the forward field single null. The equilibrium (left) indicates the plunge locations for each shot number. The SOL is demarcated with 1mm flux surfaces by the dashed and solid lines from up to $R-R_{sep} = 2.0\text{cm}$. The colorbar indicates V_p along the probe plunges, and the red arrows indicate the approximate directions of the $E_r \times B$ drifts. The profiles (right), color coded according to the sampled trajectory, show the interval averaged electron density n_e (a), electron temperature T_e (b), electron pressure P_e (c), floating potential V_f (d), plasma potential V_p (e) and Mach number $M_{||}$ (f) as a function of the flux coordinate $R-R_{sep}$. The error-bars represent the typical $\pm 2\sigma$ scatter in the data before the averages were taken.

3.2 Snowflake Divertor

Reciprocating probe data from the snowflake divertor will be compared against the SN reference in this section. It will be shown that the addition of a secondary X-point in the outer-SOL affects the radial electric field and density across the divertor leg, shedding light on why the snowflake divertor has a broader outer-target heat flux profile.

The Reversed Field snowflake equilibrium reconstruction is shown in Figure 7-left, with a dR_{x2} ^a of 3.5mm, indicated by the magenta flux surface in the equilibrium, and by the vertical dashed magenta lines at $R-R_{sep} = 3.5\text{mm}$ in (Fig 7 a-f). Three probe

^a dR_{x2} is the radial distance between the two separatrices measured at the OMP. i.e. the coordinate of the second separatrix in the flux coordinate $R-R_{sep}$

plunges in the divertor are presented and color coded for V_p (Figure 7-left) showing that V_p peaks at $R \sim 0.8m$, 5-10cm outboard of the separatrix. Figure 7e shows that the peak in V_p has been shifted all the way to the secondary separatrix such that the strong ExB drifts in the PFR-SOL boundary stretch farther into the SOL compared to the reference single null (Fig 5e) with $f_x E_r \sim 20$ kV/m. The changes in V_p correspond to changes to the V_f profiles (Fig 7d) while the T_e profiles remains relatively unchanged compared to the SN reference (Fig 7b vs Fig 5b), and still peak at the primary separatrix. The resulting ExB drifts direct particles towards the outer target in the near-SOL, and away from the outer target in the far-SOL (see red arrows in Figure 7-left). Similar to the SN reference, $M_{||}$ flows towards the outer target across the majority of the SOL but changes sign rapidly at the primary separatrix indicating flow away from the outer target (Fig 7f).

The n_e profile peak (Fig 7a) has shifted radially outward compared to the single null reaching a maximum near the secondary separatrix. Notably, n_e in the PFR is near-zero ($< 0.1e18 \text{ m}^{-3}$) in this divertor geometry, compared to $3e18 \text{ m}^{-3}$ in the Reverse Field Single Null and $18e18 \text{ m}^{-3}$ in the Forward Field Single Null. i.e. the particle convection inside the PFR drops to zero in this divertor configuration, possibly shutting down the transport between the inner and outer divertors. Parallel gradients are observed in n_e and T_e at \sim constant P_e (Fig 7a-c) which are stronger than those observed in the SN reference [compare the closest slice to the target (blue triangles) to the higher slices (black and red)].

The forward field snowflake (see equilibrium reconstruction in Figure 8-left) has a slightly larger dR_{x2} ($\sim 5mm$) than the reverse field case but has otherwise identical parameters. The secondary separatrix is marked by the magenta dashed lines in the equilibrium reconstruction in Figure 8-left and by the vertical dashed magenta lines in Figure 8a-f. Four probe plunges across the divertor are presented, two of which intersect the primary X-point.

As in the SN reference, the magnitude of V_p is lower in forward field with a higher relative scatter and uncertainty. Once again, a steep increase in V_p occurs at the primary separatrix, resulting in a $f_x E_r$ of ~ 20 kV/m. V_p is very flat in the near SOL until $R - R_{sep} > dR_{x2}$, where it begins to drop off slowly. i.e. The drifts point away from the outer target near the primary separatrix, are near zero between the separatrices, and point towards the outer target in the far-SOL as indicated by the red arrows in Figure 8-left. $M_{||}$ (Fig 8f) flows towards the outer divertor throughout the SOL, with the exception that $M_{||} < 0$ near the primary X-point which is consistent with co-Ip flow on closed flux-surfaces or with flow towards the inner target.

The n_e peaks in the forward field snowflake appear to have been shifted radially inwards into the PFR similar to the SN reference, but the probe plunges below the X-point do not penetrate deeply enough to observe the position of the peaks (Fig 8a green & black). The density peaks at the primary X-point observed for the single null case is again observed for the snowflake as well as the sharp drop in T_e (Figure 8 8b) and P_e (Fig 8c) when crossing the separatrix, consequences of which will be discussed in section 5.

The four n_e profiles in Fig 8a differ in both magnitude and shape; the two lower probe plunges (black circles, green down triangles) have a plateau with nearly constant n_e between the two separatrices ($0 < R - R_{sep} < 5mm$) while the two upper probe plunges (red up triangles, blue diamonds) have more typical n_e profile shapes that can be described by a decaying exponential function. i.e. a transition in density gradient occurs at the secondary separatrix, but only for the probe plunges which are closest to the secondary X-point.

The profiles from the snowflake divertors in reverse and forward field indicate that introducing a secondary X-point in the outer SOL spreads out the V_p gradients in the PFR-SOL boundary when compared to the reference single nulls. This reduces the peak $f_x E_r$ but allows the electric fields to extend further into the SOL, modifying the drift circulation pattern the profiles. The snowflake also shifts the positions of the peaks in n_e and V_p , and it will be shown in the next section how this affects the heat and particle fluxes.

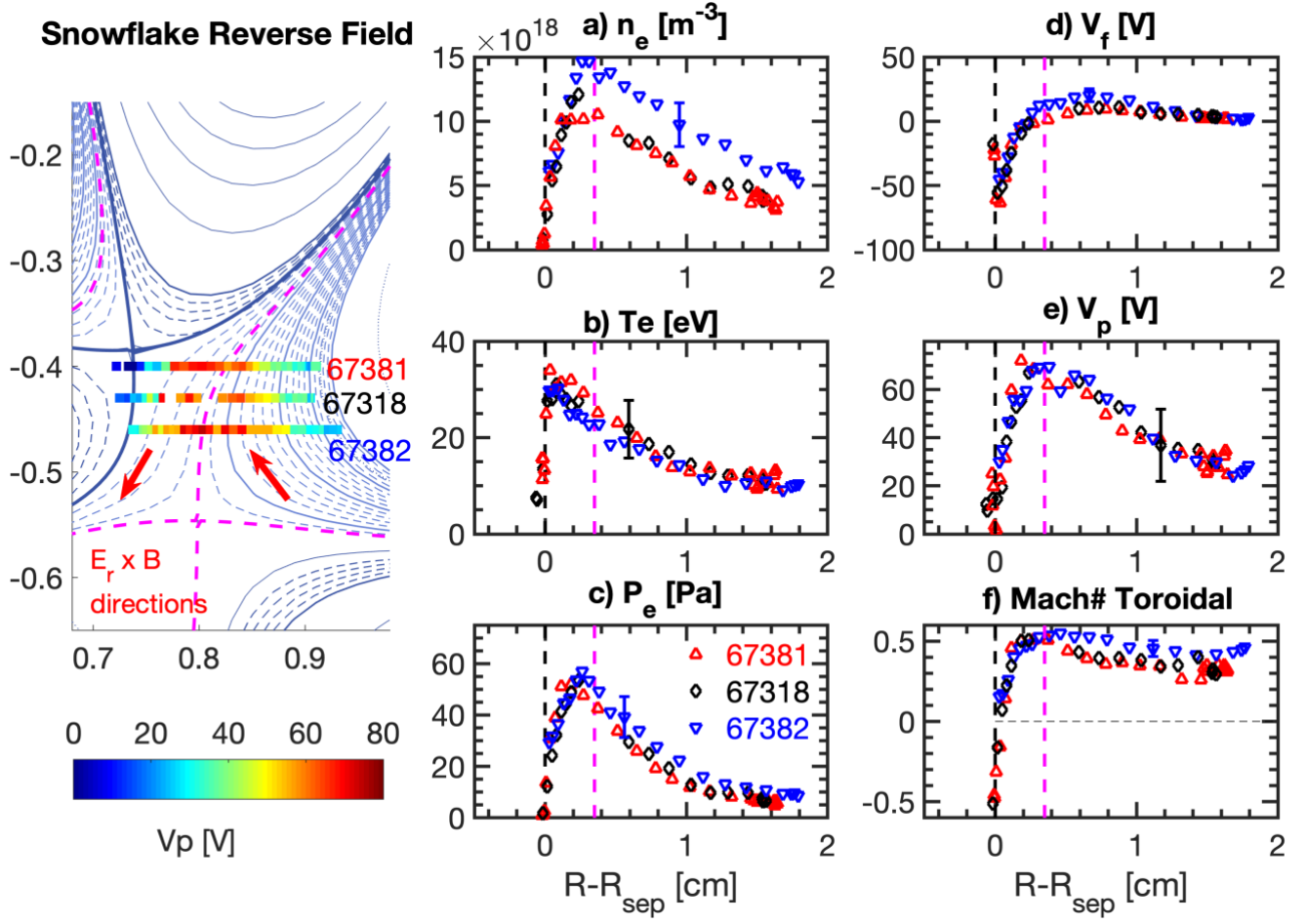


Figure 7 2D reciprocating probe profiles in the Reverse field snowflake minus. The equilibrium (left) indicates the plunge locations for each shot number. The SOL is demarcated with 1mm flux surfaces by the dashed and solid lines from up to $R-R_{sep} = 2.0\text{cm}$. The colorbar indicates V_p along the probe plunges, and the red arrows indicate the approximate directions of the $E_r \times B$ drifts. The profiles (right), color coded according to the sampled trajectory, show the interval averaged electron density n_e (a), electron temperature T_e (b), electron pressure P_e (c), floating potential V_f (d), plasma potential V_p (e) and Mach number $M_{||}$ (f) as a function of the flux coordinate $R-R_{sep}$. The error-bars represent the typical $\pm 2\sigma$ scatter in the data before the averages were taken.

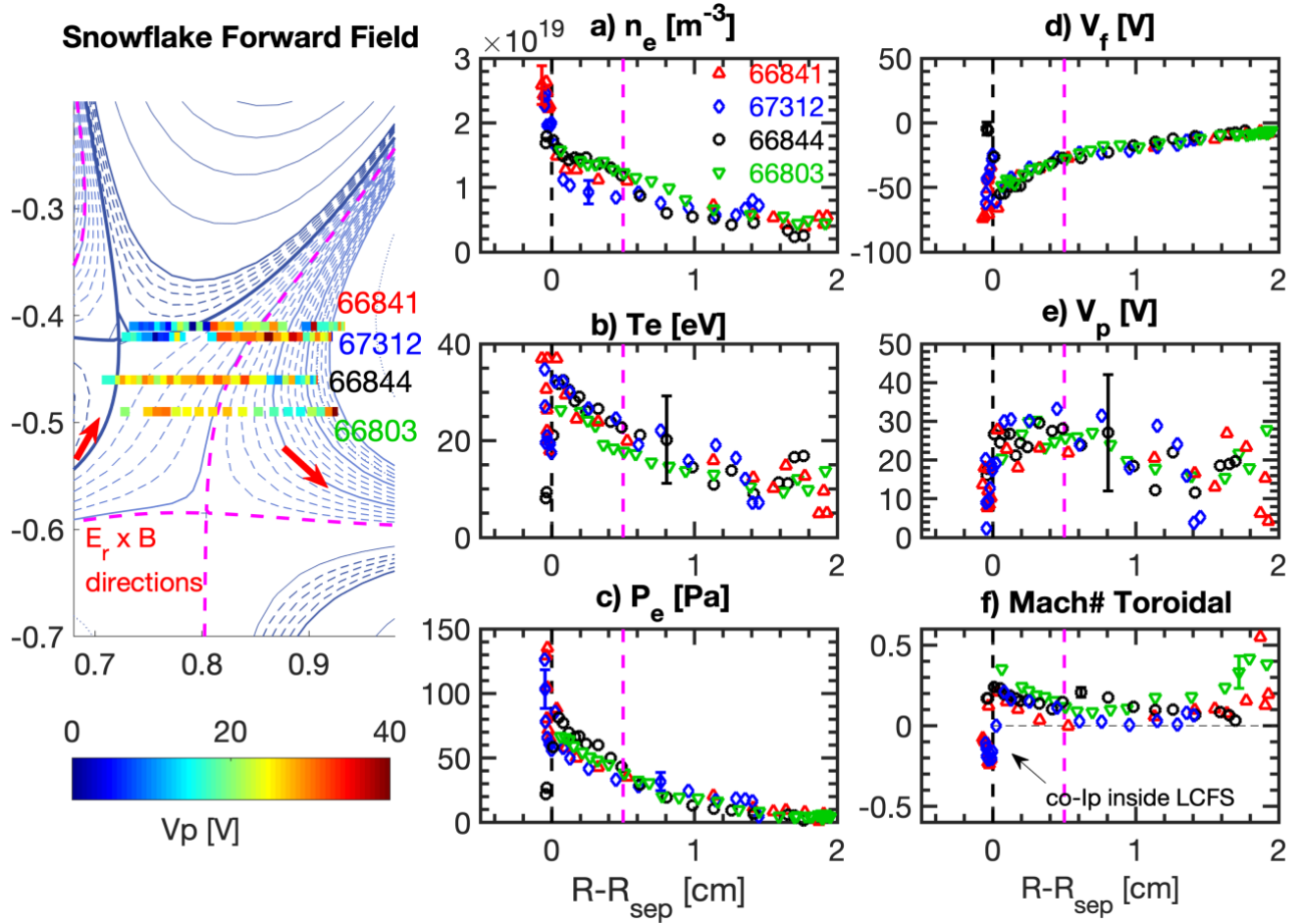


Figure 8 2D reciprocating probe profiles in the forward field snowflake minus. The equilibrium (left) indicates the plunge locations for each shot number. The SOL is demarcated with 1mm flux surfaces by the dashed and solid lines from up to $R-R_{sep} = 2.0\text{cm}$. The colorbar indicates V_p along the probe plunges, and the red arrows indicate the approximate directions of the $E_r \times B$ drifts. The profiles (right), color coded according to the sampled trajectory, show the interval averaged electron density n_e (a), electron temperature T_e (b), electron pressure P_e (c), floating potential V_f (d), plasma potential V_p (e) and Mach number $M_{||}$ (f) as a function of the flux coordinate $R-R_{sep}$. The symbols represent reciprocating probe data from the discharges as indicated in the legend. The error-bars represent the typical $\pm 2\sigma$ scatter in the data before the averages were taken.

4 Particle and Heat Convection

We now proceed to quantify the convected heat and particle fluxes for each divertor geometry and field direction with the goal of providing magnitude and context for the $E \times B$ drifts in the PFR-SOL boundary. It will be shown that the $E \times B$ drifts in this region are the dominant transport mechanism. Additionally, we will compare the integrated heat and particle fluxes from the PFR-SOL boundary drift against the total integrated fluxes at the target, and this will show that their contributions are large enough to have macroscopic effects on the divertor as a whole.

One deep probe plunge below the primary X-point was selected for each scenario for detailed analysis (the plunge locations with respect to the equilibria are shown in figs 9q-t). The profiles of V_p are shown in Fig 9a-d and are fitted using splines (red lines) which allow for the calculation of the radial electric field $f_x E_r$ (Fig 9e-h) using equation (2). $f_x E_r$ is corrected for poloidal flux expansion, and can be thought of as the E_r which would arise where $f_x=1$ (e.g. the OMP) if V_p remains constant along the field-line. The local uncorrected E_r is plotted in (Fig 9i-l) and it becomes clear that the large differences in E_r are mainly caused by geometrical effects from the variation in f_x . This is the motivation for mapping all flux terms to the OMP and correcting for flux expansion (see section 2) in lieu of comparing E_r and $v_{E \times B}$ directly. It is expected for $f_x E_r$ to be more consistent than E_r in the SOL, though the role that f_x plays in the PFR is more complex.

The ExB drifts are first contextualized using an equivalent Mach number defined as $M_{||}^{E \times B} \equiv \frac{v_{E \times B}}{c_s \tan(\alpha)}$. This term is defined such that a drift with $M_{||}^{E \times B} = 1$ will drive the same poloidal transport as a parallel flow at Mach 1. Note that only poloidal $E_r \times B$ is being considered here, and the parallel component of the drift is zero. $M_{||}^{E \times B}$, the parallel Mach number $M_{||}$, and their sum $M_{||}^{sum}$ are plotted in Figs 9m-p. Diagrams indicating drift directions with respect to the divertor geometry are shown in row 5 (Fig 9q-t).

Note that in the PFR-SOL boundary $|M_{||}^{E \times B}| \gg 1$ for all four examples with a maximum magnitude of 3.5 in the reverse field SN (Fig 9m), i.e. the transport from the ExB drift far exceeds what could be driven by a parallel flow at the sound speed. As an aside, this also indicates that the Bohm-Chodura criterion (summarized as $M_{||}^{sum} \geq 1$) [54] is satisfied even though these measurements were taken far from the target.

A strong flow-reversal is observed near the separatrix for the reverse field SN with $M_{||} = -0.5$ indicating flow away from the outer target (Fig 9m). The alignment between the strong $M_{||}^{E \times B}$ and the counteracting $M_{||} = -0.5$ suggests that the parallel flow here is a return-flow in response to pressure imbalances driven by the dominant $M_{||}^{E \times B}$ transport.

The forward field single null has a smaller peak V_p (Fig 9b) resulting in an $f_x E_r$ peak which is narrower than the reverse field case (Fig 9e-f). $M_{||}^{E \times B}$ reaches a peak of -2.7 (transport away from the outer target). $M_{||}$ is positive throughout the SOL, flowing towards the outer target. Near the separatrix, $M_{||}$ increases to 0.4, in opposition to the dominant $M_{||}^{E \times B}$ peak.

Comparing the snowflake $M_{||}^{E \times B}$ profiles against their single null references show that despite a significant distance between the primary and secondary separatrices, the snowflake divertors do affect the ExB drifts at the PFR-SOL boundary. The peak in V_p (Fig 9c-d) are shifted radially outward, and the magnitude of $f_x E_r$ are reduced compared to the reference SN divertors. In the reverse field case (Fig 9o) $M_{||}^{E \times B}$ remains positive deep into the SOL until $R-R_{sep} = 4\text{mm}$, which is deeper than the SN reference (Fig 9m). In the forward field snowflake V_p (fig 9d) reaches a peak at the secondary separatrix, unlike the SN reference (Fig 9b) which has a peak much closer to the primary separatrix.

The snowflake divertors also modify the convection throughout the SOL, where the profiles take on a more variable structure compared to the SN references. In the forward field snowflake, zero net convection is observed between the primary and secondary separatrices (Fig 9p) with a higher net convection for $R-R_{sep} < dR_{x2}$ compared to the single null reference (compare $M_{||}^{sum}$ in Fig 9p vs n), consistent with the results in [45]. In the reverse field case, the convection pattern towards the outer target is also significantly broadened compared to the single null reverse case, particularly in the region where $R-R_{sep} > 3.5\text{mm} = dR_{x2}$ (compare Fig 9o vs m). Unlike the forward field snowflake, a sudden change in convection is not observed at the secondary separatrix.

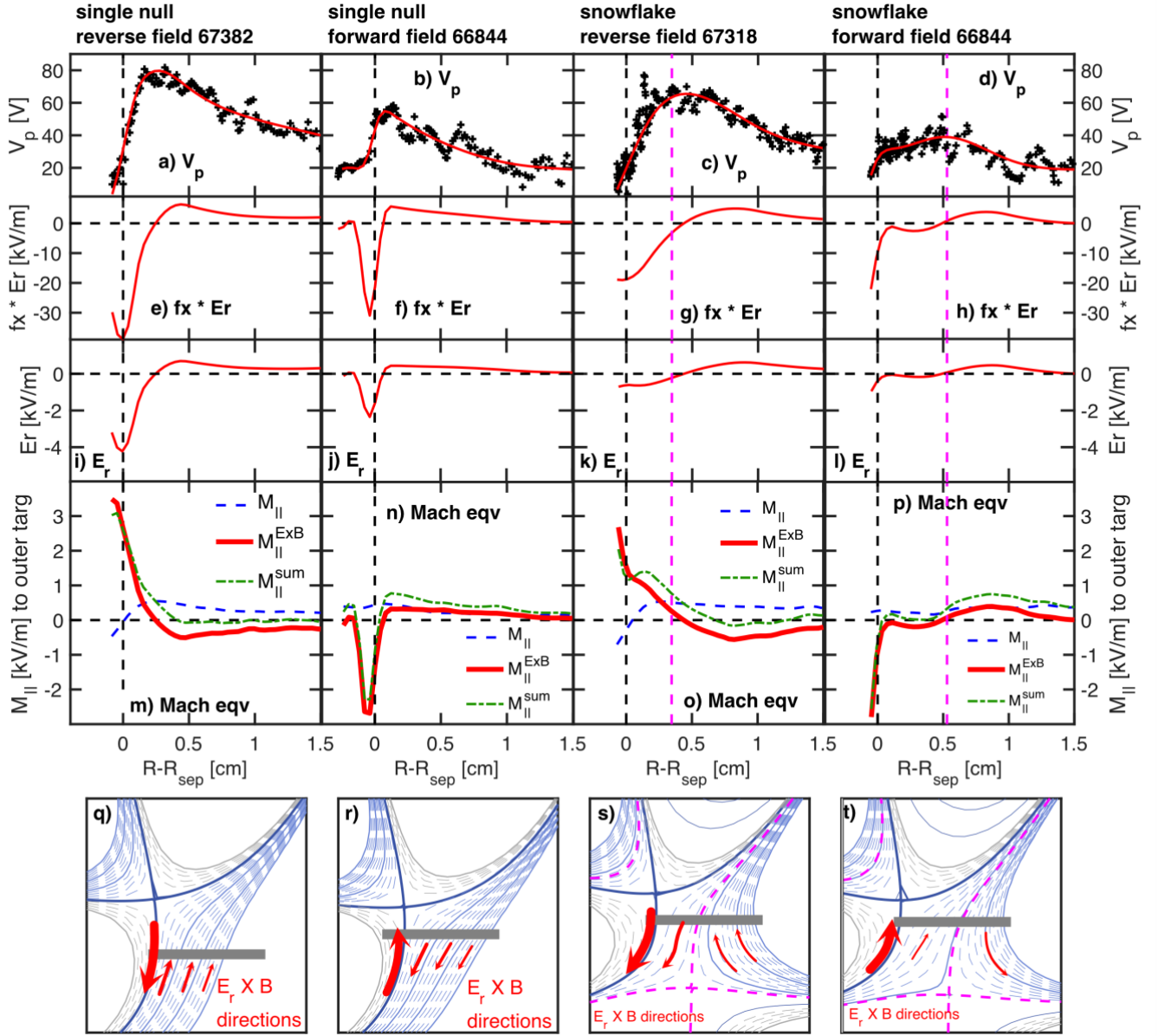


Figure 9 Electric-Field and Parallel Mach numbers in the outer divertor for the single null in forward field (column 1) the single null in reverse field (column 2) the snowflake in forward field (column 3) and the snowflake in reverse field (column 4). The plasma potential calculated over 0.5ms intervals (a-d) are fitted with splines to estimate the radial electric field with (e-h) and without (i-l) corrections for flux expansion. The equivalent Mach numbers are used to give context to the ExB transport velocities (m-p). Equilibrium diagrams (q-t) indicate where and in which directions the $E_r \times B$ occur.

While the equivalent Mach numbers show that the ExB drifts dominate over parallel convection in the PFR-SOL boundary, they tell us little about the macroscopic effects to the behavior of the divertor as a whole. More information can be obtained from the particle and heat fluxes defined in equations 1-4. In Figure 10, the projected particle fluxes $\Gamma_{\theta}^{E_r \times B}$, $\Gamma_{\theta}^{\parallel}$, and their sum $\Gamma_{\theta}^{\text{sum}}$ are plotted in row 1 (10 a-d) and the heat fluxes $q_{\theta}^{E_r \times B}$, q_{θ}^{\parallel} , and their sum q_{θ}^{sum} are plotted in row 2 (10 e-h).

The dominating fields in the PFR-SOL boundary region are visible as strong peaks in $\Gamma_{\theta}^{E_r \times B}$ and $q_{\theta}^{E_r \times B}$, but since n_e and T_e drop off rapidly towards the PFR, the flux amplitudes are affected by the radial shifts in the n_e and $f_x E_r$ profiles in the direction of the $E_{\parallel} \times B$. The peak in n_e is shifted radially outward for the reverse field SN so the peaks in $\Gamma_{\theta}^{E_r \times B}$ and $q_{\theta}^{E_r \times B}$ occur in the SOL rather than in the PFR where $M_{\parallel}^{E_r \times B}$ is highest. The peak in n_e is shifted radially inward into the PFR in the forward

field SN which improves the alignment between the peaks in $f_x E_r$ and n_e . For this reason, the forward field SN has the largest peak $\Gamma_\theta^{E_r x B}$ and $q_\theta^{E_r x B}$ magnitudes, and the peaks occur in the PFR, not the SOL, resulting in an increase in transport between the inner and outer target.

For the snowflake divertors in both field directions, the convection profiles are broader than their SN references. In the reverse field snowflake, the $\Gamma_\theta^{E_r x B}$ and $q_\theta^{E_r x B}$ peaks (Fig 10c,g) have been shifted radially outward far enough that almost no convection is measured in the PFR. The broadening is most apparent when looking at q_θ^{sum} (green dot-dashed line) where a larger fraction of the heat flux to the outer target occurs outside the secondary separatrix (Fig 10g vs Fig 10e). In the Forward Field Snowflake case (Fig 10d,h) $\Gamma_\theta^{\text{sum}}$ and q_θ^{sum} are greatly reduced between the two separatrices, and increased for R-Rsep > 5mm, which directs more heat and particles to the target outside of the secondary separatrix. These measurements are consistent with the findings that these snowflake divertors have broader outer target heat-flux footprints than the single null[44,45].

In order to investigate whether the PFR-SOL boundary drifts have a large enough contribution to have macroscopic effects on the divertor as a whole, the integrated particle flows \dot{N} and powers P (equations 5 & 6) are integrated over the areas shaded in red in Fig 10. These values are compared against the total divertor (inner + outer) integrated particle flux \dot{N}_{target} and the total divertor power P_{target} which were measured by the floor probes and the IR camera respectively. The target integrals are intended only to provide a relatively constant known quantity for comparison, not a particle or power balance. The calculations were not performed for the forward field snowflake since the probe plunges were not deep enough to map the totals for that scenario.

For the reverse field SN, $\dot{N} \cong +6.5 \times 10^{20} \text{ s}^{-1}$ and $P = +14.7 \text{ kW}$ which are equivalent to 20% \dot{N}_{target} and 17% of P_{target} . For the forward field SN, $\dot{N} \cong -10.1 \times 10^{20} \text{ s}^{-1}$ and $P = -13.4 \text{ kW}$ which are equivalent to 17% \dot{N}_{target} and 18% of P_{target} . The same exercise was carried out for the reverse field snowflake, but IR camera coverage was not available for the strike point on the outer-wall and port-protection tiles, so P_{target} was calculated using the wall Langmuir probes for that strikepoint. $\dot{N} \cong +9.5 \times 10^{20} \text{ s}^{-1}$ and $P = +20.3 \text{ kW}$ which are equivalent to 27% \dot{N}_{target} and 32% of P_{target} . While the target and PFR-SOL integrals are expected to vary significantly depending on plasma conditions, especially at higher collisionality where detachment comes into play, these values confirm that the PFR-SOL boundary drifts convect enough particles and heat to have macroscopic effects on the divertor as a whole, not just to the few millimeters over which they are active.

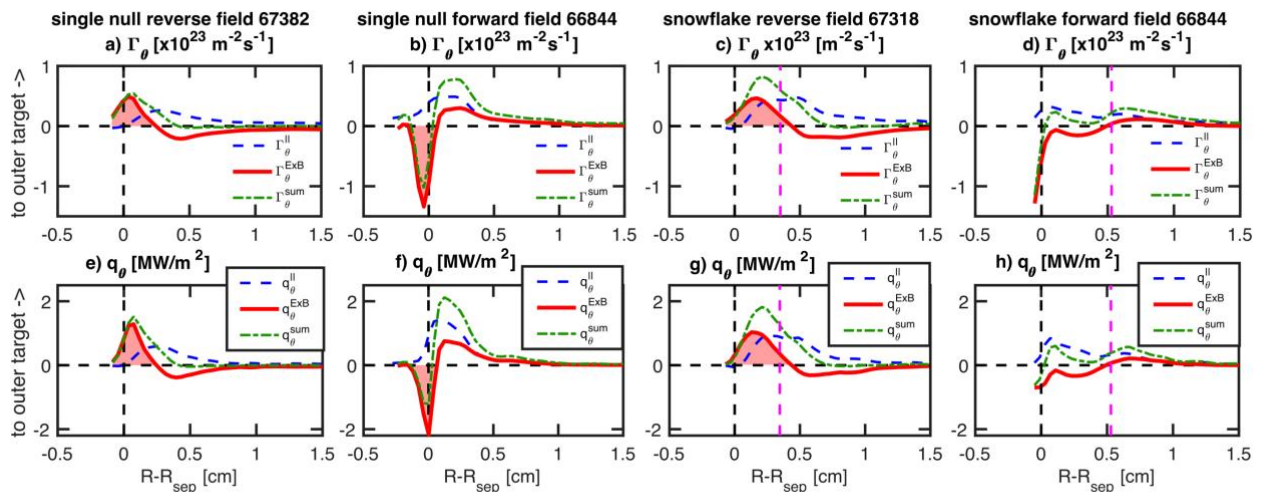


Figure 10 Corrected poloidal projections of particle (a-d) and heat (e-h) fluxes for the Single Null in Reverse Field (column 1) the Single Null in Forward Field (column 2) the Snowflake in Reverse Field (column 3) and the Snowflake in Forward Field (column 4). Positive fluxes flow towards the outer target. The shaded red regions indicate the integrated areas used to compare against the target integrated fluxes.

In summary, these results indicate that rapid ExB drifts are always present at the PFR-SOL boundary and drive poloidal transport equivalent to parallel flows around Mach 3. The largest E_r measured was 4kV/m corresponding to a drift velocity of 2.8km/s. These drifts entrain large particle and heat fluxes, equivalent to around 20% of the total target particle and heat fluxes for single null divertors in both field directions. For the reverse field snowflake, the drifts are equivalent to around 30% of the total target particle and heat fluxes. The magnitudes, radial locations, and radial extent of the PFR-SOL drifts are affected both by field direction and by divertor geometry. The Snowflake divertor was found to broaden the convection profiles in both field directions.

5 Density Peak at the primary X-point

We proceed to discuss the large peak in n_e at the primary X-point in forward field previously shown in Figure 6a and Figure 8a.

Figure 11 replots the plasma parameters against the major radius R [m] for the two probe plunges which approach the single null X-point. The average major radius of the X-point $R_{X-pt} = 0.74$ m is indicated by the dashed line. The upstream coordinate $R-R_{sep}$ is plotted in Fig 11a. The region plotted spans 8 cm in R , which corresponds to just 1.5mm upstream due to the large flux expansion near the X-point. The equilibrium reconstructions have a ± 5 mm scatter in the R_{X-pt} and Z_{X-pt} coordinates of the X-point. The blue shaded region in Fig 11a represents this uncertainty mapped to the midplane.

n_e , T_e , and electron pressure P_e are shown in Figs 11b-d for the probe plunges as well as for the upstream Thomson measurements, indicated by the magenta lines with the 2σ scatter shown by the shaded region (Thomson location shown in Figure 2). For $R > 0.78$ m, the usual relationship is observed between the upstream Thomson data and the probe data near the X-point. i.e., electron pressure balance is conserved within uncertainties while n_e is slightly higher and T_e is slightly lower near the X-point than upstream.

As the probe penetrates deeper, the n_e values increase by ~ 5 x while the T_e values decrease by ~ 4 x resulting in a P_e profile that is flat except for a clear peak at $R \sim 0.76$ m which rises ~ 2 x above the upstream TS data.

Concomitant with the P_e peak and the drop in T_e , there is a large gradient in the V_p profile (Fig 11e) that indicates the presence of an electric field near the X-point of at least 2.7 kV/m, resulting in an ExB drift ~ 1.9 km/s pointing upwards

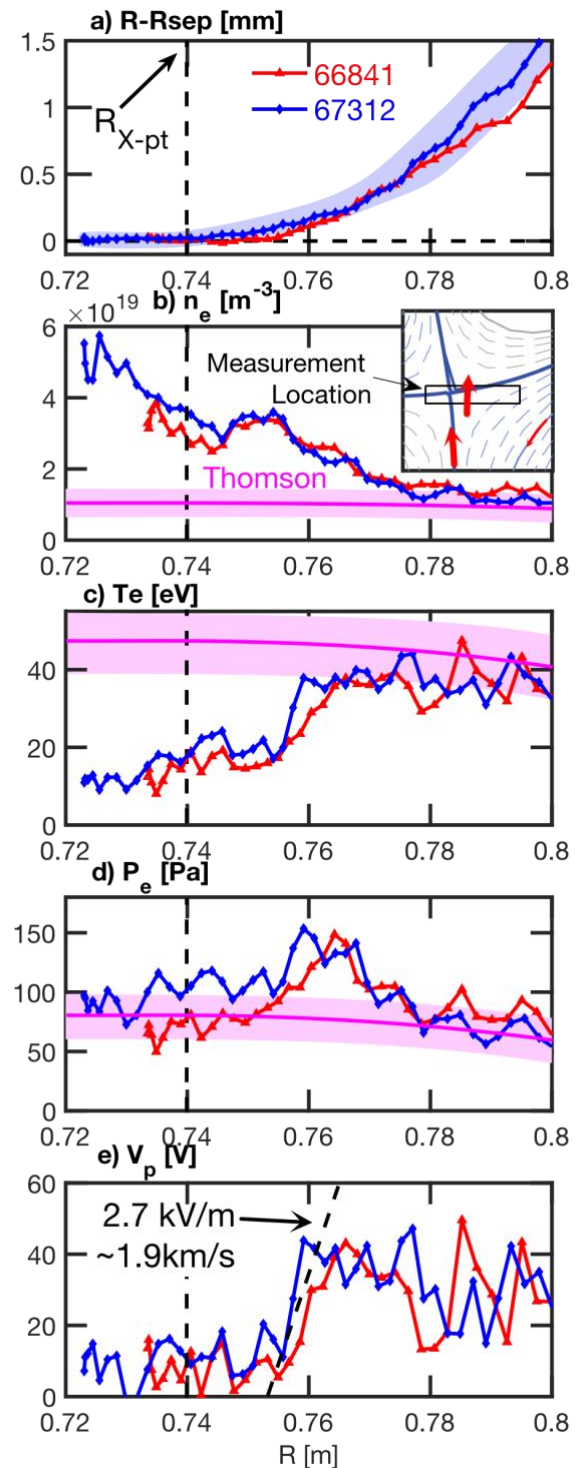


Figure 11 $R-R_{sep}$ in millimeters (a), n_e (b), T_e (c), electron pressure P_e (d) and plasma potential V_p (e) as a function of major radius R [m] for the probe plunges intersecting with the X-point in the forward-field single null. The average X-point major radius is shown by the vertical dashed line. The upstream Thomson measurements are shown by the magenta line and shaded region. The inset equilibrium reconstruction shows the region over which the data is shown. Red arrows indicate the approximate drift directions.

towards the closed flux surfaces. The direction of this ExB drift as well as those measured 3cm below the X-point are shown by the red arrows (Fig 11 inset diagram).

These results closely match previous measurements in the DIII-D X-point [13,14] where it was hypothesized that the X-point electron pressure peak was caused by high rates of ionization resulting in cold ions, a low ion pressure P_i and an elevated P_e to enforce total pressure balance. The long connection lengths near the X-point and low ion conductivity were hypothesized to allow for near zero T_i and P_i , which can explain P_e increases of up to 2x compared to upstream conditions. Both the DIII-D results and current results show regions near the X-point with low T_e and high n_e , such that the region of highest n_e is not aligned with that of highest p_e , and both results show the presence of ExB drifts which point inward towards the confined plasma at the LCFS.

This data shows that strong gradients exist in the X-point region which are not aligned with the flux surfaces. This indicates that high spatial resolution and ion cooling physics in this volume should be properly treated in simulations. E.g. recent TCX simulations [55–57] used flux-surface aligned grids with a minimum $\Delta R - R_{sep} \sim 1$ mm spacing at the separatrix that would not be sufficient to describe the gradients observed here.

6 Conclusions

Electric fields normal to the flux surfaces of ~ 4 kV/m are observed in the PFR-SOL boundary in both single null and Snowflake configurations resulting in poloidal drift velocities of up to 2.8km/s. The resulting transport is a dominating feature in both field directions with convection equivalent to a parallel flow at ~ 3 x the sound speed. The PFR-SOL boundary drifts carry an equivalent to around 20% of the total target heat and particle fluxes in the single null divertor in either field direction. In the reverse field snowflake divertor with a second x-point in the outer-SOL, the PFR-SOL boundary drift is broader and carries an equivalent to around 30% of the total target heat and particle fluxes.

The location of the PFR-SOL boundary drift is shifted radially inward towards the PFR in forward field and radially outward into the SOL in reverse field, i.e. in the $E_{||} \times B$ drift direction. The location and magnitude of these drifts are further modulated by radial shifts in the n_e profiles. In the reverse field snowflake, the aforementioned shifts are large enough that the drift-mediated heat and particle peaks are moved out of the PFR and entirely into the SOL.

Weaker fields of ~ 0.5 kV/m are observed across the common flux region of the SOL, where ExB drifts and parallel flows drive poloidal transport of similar magnitude. The snowflake divertors modify these drifts and flows resulting in wider convection profiles compared to the SN divertors. The modifications to ExB drifts were measured mainly in changes to the V_f profiles, where peak magnitudes up to 75V ($\sim 2kT_e$) were measured. The non-zero V_f measurements indicate that V_f and parallel currents should not be neglected when estimating V_p .

An electron pressure peak has been identified at the primary X-point in forward field with strong gradients in T_e and V_p across a region which maps to a very small (~ 1.5 mm) region in the midplane. The electron pressure is up to 2X higher compared to upstream measurements, consistent with a region of cold ions with near-zero ion pressure. The V_p gradient results in an electric field of ~ 2.7 kV/m, or an upward drift at 1.9km/s towards the closed flux surfaces. These results suggest that the X-point requires special treatment in fluid plasma modelling since the observed gradients are significantly smaller than the typical flux-surface aligned grid cells.

7 Acknowledgements

This work was supported by the U.S. Department of Energy under Grant No. DE-SC0010529, and by the Swiss National Science Foundation. This work has been carried out within the framework of the EUROfusion Consortium, funded by the European Union via the Euratom Research and Training Programme (Grant Agreement No 101052200 — EUROfusion). Views and opinions expressed are however those of the author(s) only and do not necessarily reflect those of the European Union or the European Commission. Neither the European Union nor the European Commission can be held responsible for them.

8 References

- [1] Eich T, Leonard A W, Pitts R a., Fundamenski W, Goldston R J, Gray T K, Herrmann A, Kirk A, Kallenbach A, Kardaun O, et al Scaling of the tokamak near the scrape-off layer H-mode power width and implications for ITER *Nucl. Fusion* **53** 093031 (2013) <https://doi.org/10.1088/0029-5515/53/9/093031>
- [2] Loarte A, Lipschultz B, Kukushkin A ., Matthews G ., Stangeby P ., Asakura N, Counsell G ., Federici G, Kallenbach A, Krieger K, et al Chapter 4: Power and particle control *Nucl. Fusion* **47** S203–63 (2007) <https://doi.org/10.1088/0029-5515/47/6/S04>
- [3] Zohm H, Angioni C, Fable E, Federici G, Gantenbein G, Hartmann T, Lackner K, Poli E, Porte L, Sauter O, et al On the physics guidelines for a tokamak DEMO *Nucl. Fusion* **53** 073019 (2013) <https://doi.org/10.1088/0029-5515/53/7/073019>
- [4] Hutchinson I H, Labombard B, Goetz J A, Lipschultz B, McCracken G M, Snipes J A and Terry J L The effects of field reversal on the Alcator C-Mod divertor *Plasma Phys. Control. Fusion* **37** 1389 (1995) <https://doi.org/10.1088/0741-3335/37/12/004>
- [5] Chankin A V. Classical drifts in the tokamak SOL and divertor: models and experiment *J. Nucl. Mater.* **241–243** 199–213 (1997) [https://doi.org/10.1016/S0022-3115\(97\)80040-2](https://doi.org/10.1016/S0022-3115(97)80040-2)
- [6] Stangeby P . and Chankin A . Simple models for the radial and poloidal $E \times B$ drifts in the scrape-off layer of a divertor tokamak: Effects on in/out asymmetries *Nucl. Fusion* **36** 839–52 (1996) <https://doi.org/10.1088/0029-5515/36/7/I02>
- [7] Krasheninnikov S I, Sigmar D J and Yushmanov P N Effect of $E \times B$ drift on divertor plasma flows *Phys. Plasmas* **2** 1972 (1998) <https://doi.org/10.1063/1.871282>
- [8] Rognlien T D, Porter G D and Ryutov D D Influence of $E \times B$ and ∇B drift terms in 2-D edge/SOL transport simulations *J. Nucl. Mater.* **266–269** 654–9 (1999) [https://doi.org/10.1016/S0022-3115\(98\)00835-6](https://doi.org/10.1016/S0022-3115(98)00835-6)
- [9] Rognlien T D, Ryutov D D, Mattor N and Porter G D Two-dimensional electric fields and drifts near the magnetic separatrix in divertor tokamaks *Phys. Plasmas* **6** 1851 (1999) <https://doi.org/10.1063/1.873488>
- [10] Rozhansky V A, Voskoboinikov S P, Kaveeva E G, Coster D P and Schneider R Simulation of tokamak edge plasma including self-consistent electric fields *Nucl. Fusion* **41** 387 (2001) <https://doi.org/10.1088/0029-5515/41/4/305>
- [11] Moyer R A, Lehmer R, Boedo J A, Watkins J G, Xu X, Myra J R, Cohen R, D'Ippolito D A, Petrie T W and Schaffer M J Potentials, $E \times B$ drifts, and fluctuations in the DIII-D boundary *J. Nucl. Mater.* **266–269** 1145–50 (1999) [https://doi.org/10.1016/S0022-3115\(98\)00618-7](https://doi.org/10.1016/S0022-3115(98)00618-7)
- [12] Boedo J A, Schaffer M J, Maingi R and Lasnier C J Electric field-induced plasma convection in tokamak divertors *Phys. Plasmas* **7** 1075 (2000) <https://doi.org/10.1063/1.873915>
- [13] Schaffer M J, Boedo J A, Moyer R A, Carlstrom T N and Watkins J G Large $E \times B$ convection near the divertor X -point *J. Nucl. Mater.* **293** 530–6 (2001)
- [14] Schaffer M J, Bray B D, Boedo J A, Carlstrom T N, Colchin R J, Hsieh C L, Moyer R A, Porter G D, Rognlien T D and Watkins J G $E \times B$ circulation at the tokamak divertor X point *Phys. Plasmas* **8** 2118–24 (2001) <https://doi.org/10.1063/1.1352597>
- [15] Radford G J, Chankin A V., Corrigan G, Simonini R, Spence J and Taroni A The Particle and Heat Drift Fluxes and their Implementation into the EDGE2D Transport Code *Contrib. to Plasma Phys.* **36** 187–91 (1996) <https://doi.org/10.1002/CTPP.2150360217>
- [16] Rozhansky V, Molchanov P, Veselova I, Voskoboinikov S, Kirk A and Coster D Contribution of $E \times B$ drifts and parallel currents to divertor asymmetries *J. Nucl. Mater.* **438** S297–302 (2013) <https://doi.org/10.1016/J.JNUCMAT.2013.01.050>
- [17] Rozhansky V, Molchanov P, Veselova I, Voskoboinikov S, Kirk A and Coster D Contribution of $E \times B$ drifts and parallel currents to divertor asymmetries *Nucl. Fusion* **52** 103017 (2012) <https://doi.org/10.1088/0029-5515/52/10/103017>
- [18] Porter G D, Petrie T W, Rognlien T D and Rensink M E UEDGE simulation of edge plasmas in DIII-D double null configurations *Phys. Plasmas* **17** 112501 (2010) <https://doi.org/10.1063/1.3499666>
- [19] Aho-Mantila L, Wischmeier M, Müller H W, Potzel S, Coster D P, Bonnin X and Conway G D Outer divertor of ASDEX Upgrade in low-density L-mode discharges in forward and reversed magnetic field: I. Comparison between measured plasma conditions and SOLPS5.0 code calculations *Nucl. Fusion* **52** 103006 (2012) <https://doi.org/10.1088/0029-5515/52/10/103006>
- [20] Chankin A ., Coster D ., Asakura N, Bonnin X, Conway G ., Corrigan G, Erents S ., Fundamenski W, Horacek J, Kallenbach A, et al Discrepancy between modelled and measured radial electric fields in the scrape-off layer of divertor tokamaks: a challenge for 2D fluid codes? *Nucl. Fusion* **47** 479–89 (2007) <https://doi.org/10.1088/0029-5515/47/5/013>
- [21] Chankin A V, Corrigan G, Groth M, Stangeby P C and contributors J Influence of the $E \times B$ drift in high recycling divertors on target asymmetries *Plasma Phys. Control. Fusion* **57** 095002 (2015) <https://doi.org/10.1088/0741-3335/57/9/095002>
- [22] Stangeby P C, Elder J D, McLean A G and Watkins J G Experimentally-based $E \times B$ drifts in the DIII-D divertor and SOL calculated from integration of Ohm's law using Thomson scattering measurements of Te and ne *Nucl. Mater. Energy* **12** 876–81 (2017) <https://doi.org/10.1016/J.NME.2017.03.021>
- [23] Christen N, Theiler C, Rognlien T D, Rensink M E, Reimerdes H, Maurizio R and Labit B Exploring drift effects in TCV single-null plasmas with the UEDGE code *Plasma Phys. Control. Fusion* **59** 105004 (2017) <https://doi.org/10.1088/1361-6587/AA7C8E>
- [24] Jaervinen A E, Allen S L, Leonard A W, McLean A G, Moser A L, Rognlien T D and Samuelli C M Role of poloidal $E \times B$ drift in divertor heat transport in DIII-D *Contrib. to Plasma Phys.* **60** e201900111 (2020) <https://doi.org/10.1002/CTPP.201900111>
- [25] Jaervinen A E, Allen S L, Eldon D, Fenstermacher M E, Groth M, Hill D N, Leonard A W, McLean A G, Porter G D, Rognlien T D, et al $E \times B$ Flux Driven Detachment Bifurcation in the DIII-D Tokamak *Phys. Rev. Lett.* **121** (2018) <https://doi.org/10.1103/PhysRevLett.121.075001>
- [26] Jaervinen A E, Allen S L, Eldon D, Fenstermacher M E, Groth M, Hill D N, Lasnier C J, Leonard A W, McLean A G, Moser A L, et al Progress in DIII-D towards validating divertor power exhaust predictions *Nucl. Fusion* **60** 056021 (2020) <https://doi.org/10.1088/1741-4326/AB7F5C>
- [27] Du H, Zheng G, Bonnin X, Li J, Xue L, Duan X and Huang W Exploring SF- in-out asymmetry and detachment bifurcation in HL-2M with $E \times B$ by SOLPS *Nucl. Mater. Energy* **22** 100719 (2020) <https://doi.org/10.1016/J.NME.2019.100719>
- [28] Porter G D, Petrie T W, Rognlien T D and Rensink M E UEDGE simulation of edge plasmas in DIII-D double null configurations *Phys. Plasmas* **17** 112501 (2010) <https://doi.org/10.1063/1.3499666>

- [29] Elder J D, McLean A G, Stangeby P C, Allen S L, Boedo J A, Bray B D, Brooks N H, Fenstermacher M E, Groth M, Leonard A W, et al OEDGE modeling of the DIII-D H-mode 13CH₄ puffing experiment *J. Nucl. Mater.* **363–365** 140–5 (2007) <https://doi.org/10.1016/j.jnucmat.2007.01.004>
- [30] Elder J D, Stangeby P C, Whyte D G, Allen S L, McLean A, Boedo J A, Bray B D, Brooks N H, Fenstermacher M E, Groth M, et al OEDGE modeling of 13C deposition in the inner divertor of DIII-D *J. Nucl. Mater.* **337–339** 79–83 (2005) <https://doi.org/10.1016/j.jnucmat.2004.10.138>
- [31] Ryutov D D Geometrical properties of a “snowflake” divertor *Phys. Plasmas* **14** 064502 (2007) <https://doi.org/10.1063/1.2738399>
- [32] Canal G P, Lunt T, Reimerdes H, Duval B P, Labit B and Vijvers W A J Enhanced E×B drift effects in the TCV snowflake divertor *Nucl. Fusion* **55** 123023 (2015) <https://doi.org/10.1088/0029-5515/55/12/123023>
- [33] Piras F, Coda S, Furno I, Moret J-M, Pitts R A, Sauter O, Tal B, Turri G, Bencze A, Duval B P, et al Snowflake divertor plasmas on TCV *Plasma Phys. Control. Fusion* **51** 055009 (2009) <https://doi.org/10.1088/0741-3335/51/5/055009>
- [34] Piras F, Coda S, Duval B P, Labit B, Marki J, Medvedev S Y, Moret J M, Pitzschke A and Sauter O “Snowflake” H mode in a tokamak plasma *Phys. Rev. Lett.* **105** 3–6 (2010) <https://doi.org/10.1103/PhysRevLett.105.155003>
- [35] Maurizio R, Duval B P, Labit B, Reimerdes H, Theiler C, Tsui C K, Boedo J, De Oliveira H, Février O, Sheikh U, et al Conduction-based model of the Scrape-Off Layer power sharing between inner and outer divertor in diverted low-density tokamak plasmas *Nucl. Mater. Energy* **19** 372–7 (2019) <https://doi.org/10.1016/J.NME.2019.03.020>
- [36] Soukhanovskii V A, Ahn J-W, Bell R E, Gates D A, Gerhardt S, Kaita R, Kolemen E, Kugel H W, LeBlanc B P, Maingi R, et al “Snowflake” divertor configuration in NSTX *J. Nucl. Mater.* **415** S365–8 (2011) <https://doi.org/10.1016/J.JNUCMAT.2010.07.047>
- [37] Soukhanovskii V A, Ahn J-W, Bell R E, Gates D A, Gerhardt S, Kaita R, Kolemen E, LeBlanc B P, Maingi R, Makowski M, et al Taming the plasma–material interface with the ‘snowflake’ divertor in NSTX *Nucl. Fusion* **51** 012001 (2011) <https://doi.org/10.1088/0029-5515/51/1/012001>
- [38] Soukhanovskii V A, Bell R E, Diallo A, Gerhardt S, Kaye S, Kolemen E, LeBlanc B P, McLean A G, Menard J E, Paul S F, et al Snowflake divertor configuration studies in National Spherical Torus Experiment *Phys. Plasmas* **19** 082504 (2012) <https://doi.org/10.1063/1.4737117>
- [39] Soukhanovskii V A, Allen S L, Fenstermacher M E, Lasnier C J, Makowski M A, McLean A G, Meier E T, Meyer W H, Rognlien T D, Ryutov D D, et al Snowflake Divertor Experiments in the DIII-D, NSTX, and NSTX-U Tokamaks Aimed at the Development of the Divertor Power Exhaust Solution *IEEE Trans. Plasma Sci.* **44** 3445–55 (2016) <https://doi.org/10.1109/TPS.2016.2625325>
- [40] Porter G D, Petrie T W, Rognlien T D and Rensink M E UEDGE simulation of edge plasmas in DIII-D double null configurations *Phys. Plasmas* **17** 112501 (2010) <https://doi.org/10.1063/1.3499666>
- [41] Lunt T, Zohm H, Herrmann A, Kallenbach A, Dunne M, Feng Y, Neu R and Wischmeier M Proposal of an alternative upper divertor in ASDEX Upgrade supported by EMC3-EIRENE simulations *Nucl. Mater. Energy* **12** 1037–42 (2017) <https://doi.org/10.1016/J.NME.2016.12.035>
- [42] Lunt T, Canal G P, Duval B P, Feng Y, Labit B, McCarthy P, Reimerdes H, Vijvers W A J and Wischmeier M Numerical study of potential heat flux mitigation effects in the TCV snowflake divertor *Plasma Phys. Control. Fusion* **58** (2016) <https://doi.org/10.1088/0741-3335/58/4/045027>
- [43] Lunt T, Canal G P, Feng Y, Reimerdes H, Duval B P, Labit B, Vijvers W A J J, Coster D, Lackner K and Wischmeier M First EMC3-Eirene simulations of the TCV snowflake divertor *Plasma Phys. Control. Fusion* **56** 035009 (2014) <https://doi.org/10.1088/0741-3335/56/3/035009>
- [44] Maurizio R, Tsui C K, Duval B P, Reimerdes H, Theiler C, Boedo J A, Labit B, Sheikh U, Spolaore M, Team T T Euro M, et al The effect of the secondary x-point on the Scrape-Off Layer transport in the TCV Snowflake Minus divertor *Nucl. Fusion* **59** 016014 (2019) <https://doi.org/10.1088/1741-4326/aaee1b>
- [45] Tsui C K, Boedo J A J A, Galassi D, Loizu J, Maurizio R, Reimerdes H, Duval B P B P, Février O, Spolaore M, Wensing M, et al Parallel convection and E × B drifts in the TCV snowflake divertor and their effects on target heat-fluxes *Nucl. Fusion* **61** 046004 (2021) <https://doi.org/10.1088/1741-4326/abdb93>
- [46] Hofmann F, Lister J B, Anton W, Barry S, Behn R, Bernel S, Besson G, Buhlmann F, Chavan R, Corboz M, et al Creation and control of variably shaped plasmas in TCV *Plasma Phys. Control. Fusion* **36** B277 (1994) <https://doi.org/10.1088/0741-3335/36/12B/023>
- [47] Hawke J, Andrebe Y, Bertizzolo R, Blanchard P, Chavan R, Decker J, Duval B, Lavanchy P, Llobet X, Marlétaz B, et al Improving spatial and spectral resolution of TCV Thomson scattering *J. Instrum.* **12** C12005 (2017) <https://doi.org/10.1088/1748-0221/12/12/C12005>
- [48] De Oliveira H, Marmillod P, Theiler C, Chavan R, Février O, Labit B, Lavanchy P, Marlétaz B, Pitts R A and team T Langmuir probe electronics upgrade on the tokamak à configuration variable *Rev. Sci. Instrum.* **90** 083502 (2019) <https://doi.org/10.1063/1.5108876>
- [49] Février O, Theiler C, De Oliveira H, Labit B, Fedorczak N and Baillod A Analysis of wall-embedded Langmuir probe signals in different conditions on the Tokamak à Configuration Variable *Rev. Sci. Instrum.* **89** 053502 (2018) <https://doi.org/10.1063/1.5022459>
- [50] Boedo J A, Crocker N, Chousal L, Hernandez R, Chalfant J, Kugel H, Roney P and Wertenbaker J Fast scanning probe for the NSTX spherical tokamak *Rev. Sci. Instrum.* **80** 123506 (2009) <https://doi.org/10.1063/1.3266065>
- [51] Hutchinson I H *Principles of Plasma Diagnostics: Second Edition* vol 44 (Cambridge University Press) (2002) <https://doi.org/10.1088/0741-3335/44/12/701>
- [52] Helander P and Sigmar D J *Collisional transport in magnetized plasmas* (Cambridge University Press) (2002) <https://doi.org/10.1017/cbo9780511770609.006>

- [53] Smick N, LaBombard B and Hutchinson I H Transport and drift-driven plasma flow components in the Alcator C-Mod boundary plasma *Nucl. Fusion* **53** 023001 (**2013**) <https://doi.org/10.1088/0029-5515/53/2/023001>
- [54] Stangeby P C The Bohm-Chodura plasma sheath criterion *Phys. Plasmas* **2** 702–6 (**1995**) <https://doi.org/10.1063/1.871483>
- [55] Fasoli A, Reimerdes H, Alberti S, Baquero-Ruiz M, Duval B P, Havlikova E, Karpushov A, Moret J M, Toussaint M, Elaian H, et al TCV heating and divertor upgrades *Nucl. Fusion* **60** 016019 (**2020**) <https://doi.org/10.1088/1741-4326/ab4c56>
- [56] Wensing M, Duval B P, Février O, Fil A, Galassi D, Havlickova E, Perek A, Reimerdes H, Theiler C, Verhaegh K, et al SOLPS-ITER simulations of the TCV divertor upgrade *Plasma Phys. Control. Fusion* **61** 085029 (**2019**) <https://doi.org/10.1088/1361-6587/ab2b1f>
- [57] Galassi D, Reimerdes H, Theiler C, Wensing M, Bufferand H, Ciraolo G, Innocente P, Marandet Y and Tamain P Numerical investigation of optimal divertor gas baffle closure on TCV *Plasma Phys. Control. Fusion* **62** 13 (**2020**) <https://doi.org/10.1088/1361-6587/abb24f>